J Mater Sci (2011) 46:4638–4645
DOI 10.1007/s10853-011-5366-2

Morphological and magnetic properties of $TiO_2/Fe_{50}Co_{50}$ composite films

A. Kulkarni · V. S. K. Chakravadhanula · V. Duppel · D. Meyners · V. Zaporojtchenko · T. Strunskus · L. Kienle · E. Quandt · F. Faupel

Received: 28 August 2010 / Accepted: 3 February 2011 / Published online: 19 February 2011

Abstract Nanocomposites of FeCo and TiO_2 with wide range of metal volume fractions (MVFs) were prepared by co-sputtering. High resolution transmission electron microscopy analysis reveals that the microstructure of the nanocomposites depends on the MVF which determines the particle size and separation. FeCo nanoparticles are amorphous at lower MVF whereas crystallites are present at higher MVF. Likewise, the magnetic characteristics of these films depend on the MVF. At low MVF, composite films exhibit superparamagnetism whereas at high MVF, coalescence of crystalline nanoparticles results in the opening up of hysteresis loop. These composite films show a considerable room temperature tunnel magnetoresistance and being proportional to the square of the normalized magnetization $(M/M_s)^2$.

A. Kulkarni · V. Zaporojtchenko · T. Strunskus · F. Faupel (✉)
Institute for Materials Science—Multicomponent Materials, Faculty of Engineering, University of Kiel, Kaiserstr. 2, 24143 Kiel, Germany
e-mail: ff@tf.uni-kiel.de

A. Kulkarni
e-mail: ak@tf.uni-kiel.de

V. S. K. Chakravadhanula · L. Kienle
Institute for Materials Science—Synthesis and Real Structures, Faculty of Engineering, University of Kiel, Kiel, Germany

D. Meyners · E. Quandt
Institute for Materials Science—Inorganic Functional Materials, Faculty of Engineering, University of Kiel, Kiel, Germany

V. Duppel
Max Planck Institute for Solid State Research, Heisenbergstr. 1, 70569 Stuttgart, Germany

Introduction

Metal-dielectric nanocomposites are of extensive research interest due to their remarkable physical and chemical properties. Among them, composites with magnetic nanoparticles are of particular attraction, since the discovery of tunnel magnetoresistance (TMR) in granular films [1, 2]. These composites have applications in spintronics [3] and GHz rf circuits [4]. In relation to the metal volume fraction (MVF), they exhibit three electrical regimes; dielectric, transition and metallic, with each regime having distinct properties. Composites typically containing 30–40% MVF show superparamagnetism and a room temperature (RT) tunnel magnetoresistance which arises from tunneling of spin-polarized electrons [5, 6]. The magnetic behavior of these composites is of complex nature governed by the topological structure of the ferromagnetic component. Size of nanoparticles [7] and inter-particle separation which depends on the metal volume fraction and on the matrix are key aspects. Some authors have reported the finding of amorphous particles, along with crystalline phase, in oxides such as Al_2O_3 [8], SiO_2, and in multilayer configuration of Co/TiO_2 [9].

Here, we report the changes in the microstructure of metallic nanoparticles embedded in TiO_2 matrix from amorphous to crystalline in relation to MVF. TiO_2 was chosen as matrix because so far it was only investigated in multilayer configuration but not in a granular system. Tunnel magnetoresistance and magnetization behavior of these composites with respect to the MVF will also be

discussed. Further, the particle size and its distribution, key parameters for the reported phenomena are derived from the Langevin function.

Experimental details

Composite films of TiO_2/FeCo were sputter deposited at RT in an argon atmosphere on a copper TEM grid, and a specially designed Si/SiO_2 substrate for TMR measurement. A compositional spread was achieved within one deposition by co-sputtering from two sources. The sources were mounted at 30° with respect to normal, and the sample holder was centrally mounted and held stationary. By using this effect, in one sputtering process as many as five samples with distinct MVF were fabricated. The base pressure was lower than 5×10^{-7} mbar, FeCo was sputtered by a DC magnetron source and TiO_2 by a RF magnetron source. The substrates for TMR were prepared by photolithography with Au/Cr electrodes of 30/5 nm thickness and an interspacing of 25 µm (inset Fig. 7). The tunnel resistance was measured across the interspacing. Two quartz crystal microbalances were used to monitor the individual in situ deposition rates, vital to control the required filling factor and film thickness. The thickness of films for transmission electron microscopy and TMR measurement were about 40 nm and 250 nm, respectively.

Morphology and structural variation dependence on the MVF were studied by HRTEM with a Tecnai F30 G^2 ST (FEG, 300 kV, $C_S = 1.2$ mm) and a Philips CM 30 ST microscope (LaB_6 cathode, 300 kV, $C_S = 1.15$ mm). All images were recorded with Gatan Multiscan CCD cameras and evaluated with the programs Digital Micrograph 3.6.1 (Gatan) or Crisp (Calidris). Selected area electron diffraction (SAED) was carried out using a diaphragm which limited the diffraction to a circular area of 250 nm in diameter. Chemical analysis by an energy dispersive X-ray spectrometer (EDX) was performed in the nanoprobe mode and by spectral imaging (scanning mode) with a Si/Li detector (Noran, Vantage System). The films stored under ambient conditions for 2 months were named as aged films. Heating experiments were performed in situ within the Tecnai F30 G^2 by using a double-tilt Tantalum heating stage holder (Gatan).

Magnetization curves of the samples were measured by a vibrating sample magnetometer (VSM) at RT. TMR measurements were performed by a two probe method at RT. The film thickness, which is the step height between masked and unmasked area on the substrate, was measured by a surface profilometer. The metal volume faction was determined [10, 11] by EDX.

Results and discussion

Structural properties

TEM analyses reveal full information about chemistry and structure of the composite material. The structural ordering of FeCo particles incorporated inside the amorphous TiO_2 matrix depends on the MVF. Nanoscale FeCo crystallites were observed at higher MVF. Figure 1a and b show the HRTEM micrograph recorded on a freshly prepared composite film with MVF $\sim$ 38% and the particle size distribution from the corresponding sample respectively. The lattice fringes matched to the structure of FeCo as demonstrated by the accompanying Fourier transforms which were calculated inside the marked areas, e.g., d(011) = 0.204(10) nm, d(002) = 0.141(10) nm (reference values [12, 13]: 0.203 nm, 0.143 nm). For MVF $< 35\%$, the FeCo

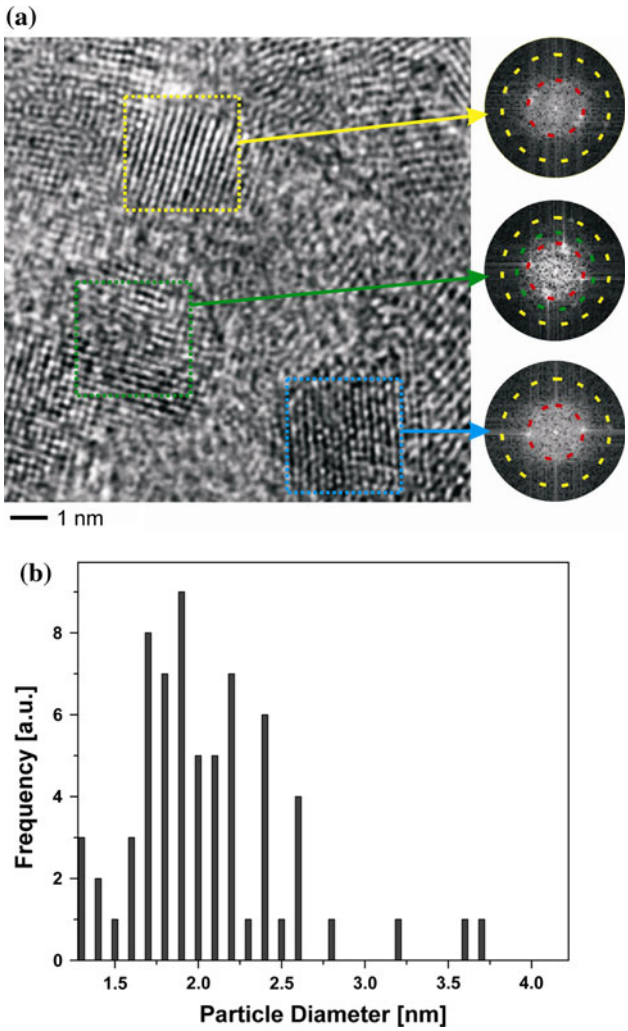

Fig. 1 **a** HRTEM micrograph of the nanocomposite (38% MVF) with the Fourier transforms from the marked nanoparticles showing the lattice fringes $d(011) = 0.204(10)$ nm, $d(002) = 0.141(10)$ nm and **b** the particle size distribution from the corresponding sample

particles are amorphous, cf., the diffracted intensity on a broad concentric circle at $d \sim 0.20(1)$ nm in Fig. 2a, left. The HRTEM micrographs (e.g., Fig. 2a, right) display no structural ordering even at the nanoscale; thus, the material does not contain any crystalline component of significant dimension. EDX nanoprobe-analyses indicate an equi-atomic ratio of Fe:Co in all transmittable areas under investigation. Further EDX analyses focus on the oxygen content of the samples. In spite of the well-known problems of the light elements' quantification by EDX, test measurements on distinct oxide materials point to a sufficient reliability of our setup for a semi-quantitative interpretation, even in such critical field. In the case of freshly prepared composite films, the quantification of the data gives a ratio O:Ti between 1.8 and 2.5. Scanning transmission electron microscopy (STEM) has been employed to obtain EDX-elemental maps of the nanocomposites. At room temperature, the Fe and Co maps as well as the Ti and O maps correlate quiet well. This analysis shows that areas rich in Ti are rich in O (poor in Fe and Co). In addition areas rich in Fe are rich in Co (poor in Ti and O, Fig. 2c). Hence, the chemical nature of these freshly prepared films corresponds to a composite material made of FeCo and TiO_2.

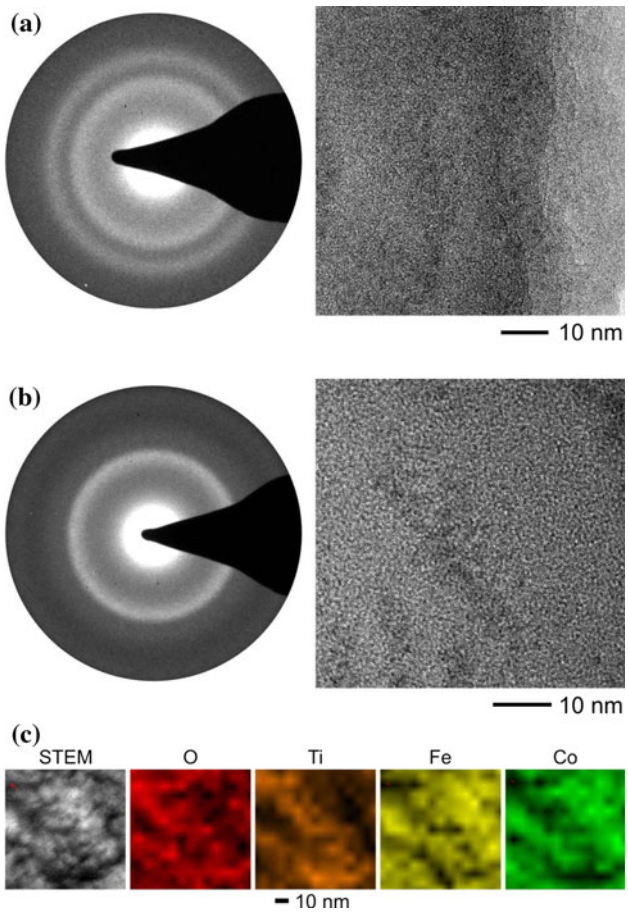

Fig. 2 SAED patterns (each *left*) and bright-field images (each *right*) of (**a**) freshly prepared, (**b**) aged nanocomposite films (MVF ~25–30%). **c** STEM image (*left*) and EDX elemental maps

In contrast, EDX analyses on films (MVF ~25–30%) which were stored in air for 2 months indicate an increase of the oxygen content, thus implying the presence of highly oxidized and thus fully ceramic material (labeled "aged films"). In case of the aged films with low MVF, all components are again fully amorphous as supported by bright-field images exhibiting no diffraction contrast and HRTEM (Fig. 2b, right). Just very broad diffuse intensity concentrating on a concentric circle is seen in the SAED pattern (Fig. 2b, left). The diameter of the circle was determined to be $d \sim 0.27(1)$ nm. The aged films appear chemically and optically homogeneous, and like for the freshly prepared films, the equiatomic ratio of Fe and Co is well adjusted even at the nanoscale. EDX nanoprobe-analyses (average of five point measurements, distinct areas) display the homogeneity of the material by the low variance of the metal content, Ti:Fe:Co = 43.1(7) at.%:28.3(5) at.%:28.7(1.4) at.%. Thus, aging of the films does not produce a detectable segregation of distinct phases. Based on the ceramic nature of the films, the atomic ratio of O:Ti was significantly larger than the expected value of 2.0 for a freshly prepared composite, namely in the range of 3.3–3.8. Hence, Fe and Co must be incorporated in an oxidized form inside the materials to meet the criterion of charge balance. Assuming Fe and Co in tri- and bivalent states, the charge balance is approximately met by the average composition close to $Co_{0.56}Fe_{0.56}Ti_{0.8}O_3$. Such finding confirmed the formation of a homogeneous ceramic film from an amorphous composite by aging. The degradation of the material has no significant influence on the functional properties. Thus, we concluded that the aging is restricted to a thin surface layer which protects the internal areas of thicker films against further oxidation.

The presence of amorphous FeCo at low MVF raised the question about the chemical nature of the crystalline products initially produced by heating. Since the films do not change their microstructure during electron beam impact, in situ heating represents the method of choice for the investigation. At a temperature of 450°C, a separation of the bright field contrast by the formation of nanosized crystallites with strong diffraction contrast was observed (Fig. 3a). These species are embedded inside the amorphous matrix and are frequently facetted, e.g., enlarged section in Fig. 3a. EDX analyses performed on the strongly diffracting crystallites indicate a considerable decrease of the Fe:Co ratio to typical values in the range of 0.05–0.1, while in the surrounding matrix only traces of Co can be detected. This finding can be rationalized by assuming Co as the initially formed crystalline phase. The SAED patterns of Fig. 3b and c were recorded on single and multiple

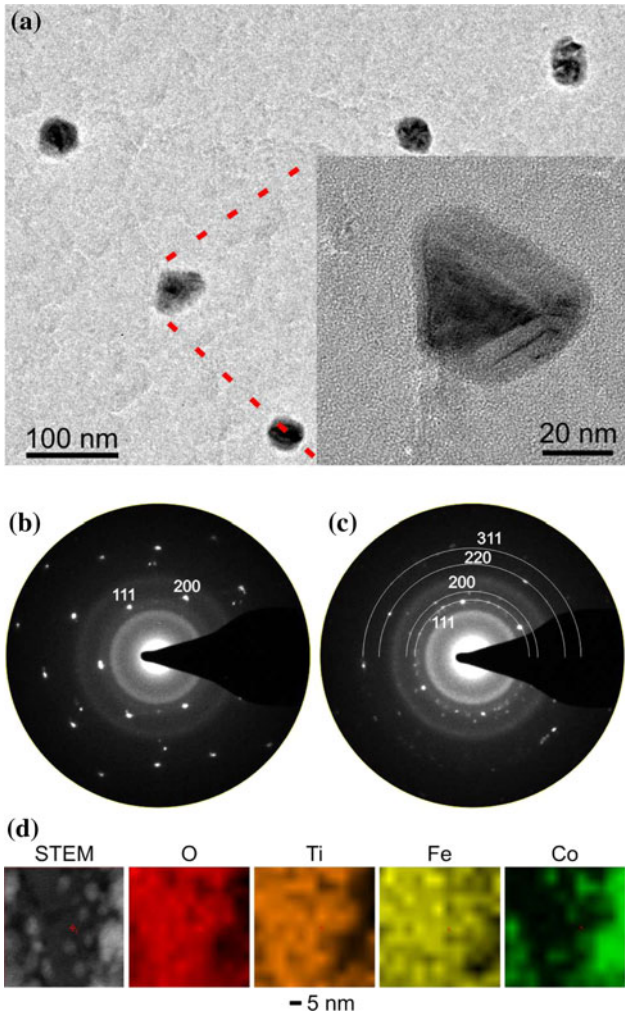

Fig. 3 **a** Microstructure of the initially amorphous film TiO_2/FeCo after in situ heating. *Inset*: enlarged section of a Co nanocrystal. **b** SAED patterns recorded on a single nanocrystal, [110], and **c** on multiple crystals of fcc-cobalt. The *d* values of $d(111) = 0.205(5)$ nm and $d(200) = 0.178(5)$ nm (**b**) and $d(111) = 0.205(5)$ nm; $d(200) = 0.178(5)$ nm, $d(220) = 0.126(5)$ nm, $d(311) = 0.107(5)$ nm (**c**) convincingly agree with the reference values. **d** STEM image (*left*) and EDX elemental maps recorded after in situ heating

crystallites, respectively. All *d* values agree well with the reference values [14] for the cubic high temperature modification of Co. As exemplified by the HRTEM analysis, the initially formed Co crystals contain crystal defects. It is not clear whether such features are interrelated with strain or local changes of the chemical composition, e.g., a partial oxidation of Co. In addition, Fig. 3d depicts the STEM-EDX elemental maps which confirm the segregation of Co after the in situ heating. The TMR in heated samples (MVF ~25–30%) vanishes, due to a huge increase in the mean particle distance and phase separation of iron and cobalt, obvious from the TEM analysis.

The finding of amorphous FeCo nanoparticles is very interesting from the fundamental point of view because FeCo is not expected to be a glass forming alloy even at high quenching rates. The amorphous structure seems to be a result of the very small particle size and the resulting interfacial stress which can better be accommodated by an amorphous structure.

Moreover, the magnetic behavior showing the characteristics of magnetic single-domain particles and superparamagnetism along with the TMR results, demonstrate spin-dependent tunneling between well separated magnetic particles give further evidence of the presence of distinct FeCo particles (see below). We note that amorphous particles were also observed in other oxide matrices such as Al_2O_3 [9].

Magnetic properties

Figure 4 shows in-plane magnetization curves measured at RT for TiO_2/FeCo granular films. The granular films with MVF fraction <50% exhibit superparamagnetism, with vanishing magnetization at H = 0. According to previous works, this is a typical behavior for such granular films [15, 16]. The superparamagnetic behavior requires well-separated magnetic particles. In contrast, the composite films with 53% MVF are ferromagnetic with coercive field of 60 Oe. The VSM measurements indicate that with an increase in the MVF, the composite films transit from superparamagnetic to ferromagnetic. This is reflected in a much higher permeability. The increase in saturation magnetization measured at Hmax = 7.5 KOe with increasing MVF could be partially due to incomplete saturation of the superparamagnetic films at RT and to the formation of a thin oxide shell which has less influence on larger particles. As mentioned earlier, FeCo forms coalesced crystallites in the TiO_2 matrix at higher filling factors resulting in the opening

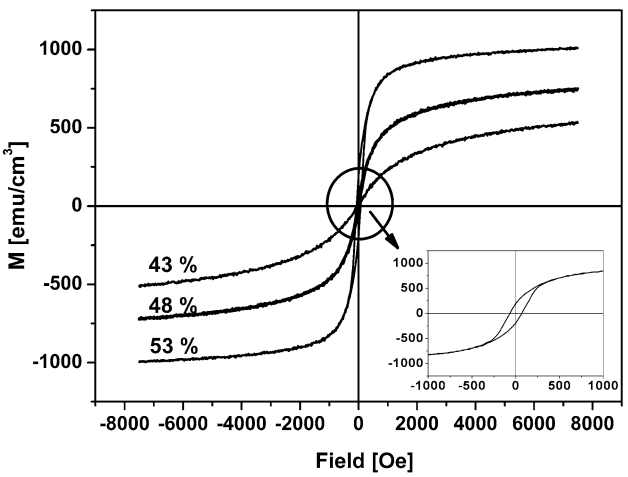

Fig. 4 In plane magnetization curves of TiO_2/FeCo measured at RT for various MVFs as indicated. The inset shows the magnified view of hysteresis loop for 53% MVF

up of the hysteresis loop. Here, the magnetization process is governed by domain wall motions whereas magnetization reversal can only occur via rotational processes in the composites containing well-separated single domain particles [17]. The critical particle size at which the change from superparamagnetic to ferromagnetic behavior occurs is an interesting information. Particle size can be qualitatively derived by fitting the experimental magnetization curve with classical Langevin function [18]. It describes the magnetization in superparamagnetic state by

$$\frac{M}{M_o} = L(\alpha) = \coth\left(\frac{\mu H}{k_B T}\right) - \left(\frac{k_B T}{\mu H}\right)$$

$$\mu = M_s V = M_s \frac{4\pi}{3}\left(\frac{d}{2}\right)^3$$

where M_o is the saturation magnetization of the sample at a given temperature T, M_s saturation magnetization of the bulk phase, H is the applied field and the particle diameter is given by d. It is a known fact that the particle size d has a certain distribution and it was shown earlier that it tends to follow a log normal distribution function [19] defined by

$$P(d) = \frac{1}{\sqrt{2\pi}\ln\sigma}\exp\left(\frac{(\ln d - \ln dm)^2}{2\ln^2\sigma}\right),$$

where dm and σ are statistical median and standard deviation, which describe the probability distribution function $P(d)$. Here the measured curves are fitted to the Langevin function by least square approach. Figure 5 shows the calculated magnetization as a function of the applied field and the particle size distribution function which gives best fit. The average particle size and the width of the distribution increases, as the metal volume fraction increases. This is also the characteristic of the deposition technique. According to domain theory and experiments [20] on ultra fine particles, the maximum coercivity was reached when the radii were 21 nm and 20 nm for Fe and Co, respectively. The transition to the superparamagnetic regime occurs below these dimensions ($r < 10$ nm). Estimations of critical size for spherical particles with no shape anisotropy made by Kittel as mentioned in the reference [21] were also in the same range. In our case, the average particle diameter for 48% MVF is 5.3 nm and the distribution function has large tail toward the end. Further increase in the MVF is bound to increase the d and width. This point marks the commencement of opening up of hysteresis loop, and hence it can be said that the change in the magnetization behavior occurs above diameter 5.3 nm. It should be noted that as the filling factor increases the clusters come closer and there exist a possibility of coalescence.

The particle size distribution obtained from TEM for 38% volume fraction is 2 nm, which is inline with the observation made here. Therefore, one can say that the

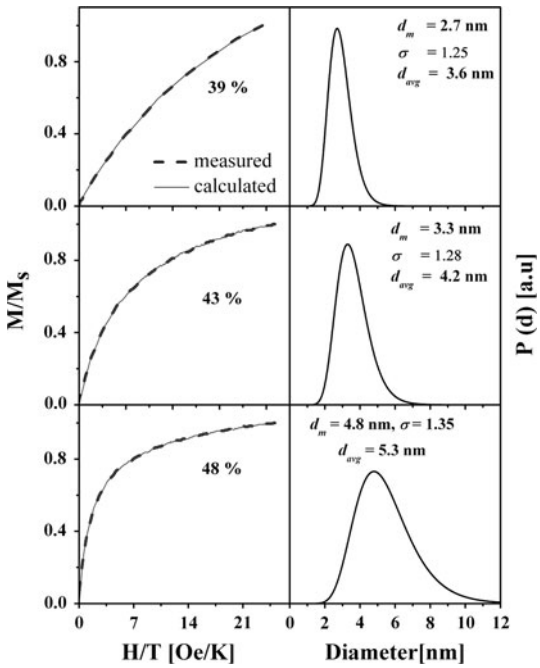

Fig. 5 Calculated magnetization curves (*solid line*) from Langevin function and the corresponding particle size distribution which gives the best fit, for different MVF

average particle size for filling factor <38% might be less than 2 nm and some of the metal present could be still in atomic form.

Transport properties

The type of electrical transport mechanism in the composites is closely related to the morphology of the composites. TMR should occur in a region where the electrical conductivity shows tunnel type transport mechanism. This can be verified by measuring the temperature dependence of electrical resistance. Such a measurement is shown in Fig. 6. The temperature coefficient of resistance is negative for 43 and 48% MVF, suggesting non metallic conductivity. It shifts to positive values for 53% above 150 K, indicating the onset of metallic behavior due to percolation. For 53% MVF, the resistance reaches to a minimum value at 150 K before climbing up again, this could be due to multiple transport mechanisms or the semiconducting behavior of the matrix. For metal–insulator composites, Helamn and Abeles [2] observed, that the temperature dependence of resistance should follow an exponential law involving temperature T and activation energy C responsible for the process.

$$R \sim \exp\left(\sqrt{C/k_B T}\right)$$

As shown in Fig. 6c, a logarithm of R plot is approximately linear to $T^{-0.5}$ for 43 and 48%. These measurements

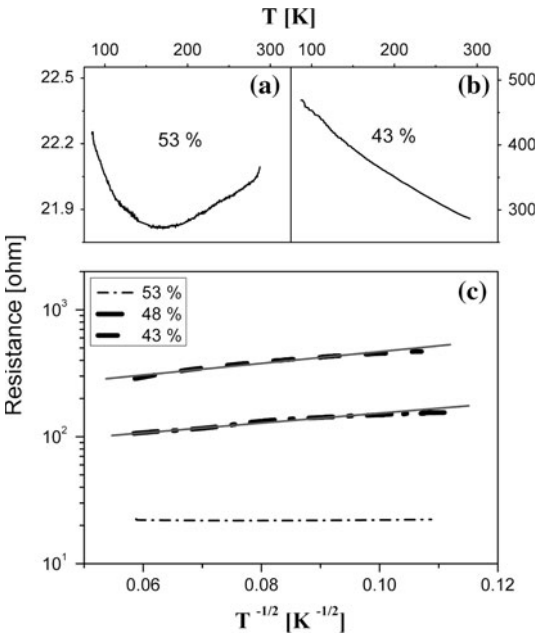

Fig. 6 Relationship between temperature and electrical resistance for MVF: **a** 53%, **b** 43%, and **c** plotted in log $R - T^{-1/2}$ scale. The *solid lines* in **c** are approximate fit to $\log(R) \sim \exp(C/T)^{-1/2}$

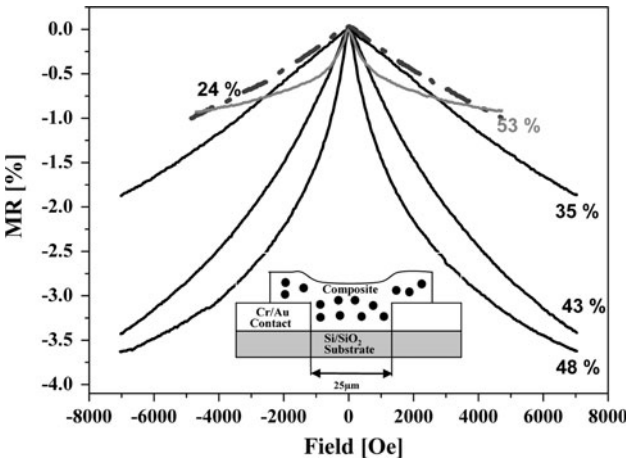

Fig. 7 Dependence of electrical resistance on the applied magnetic field at RT for $Fe_{50}Co_{50}$–TiO_2 composite with different MVF as indicated

correlate well with the fact that the maximum of the magnetoresistance corresponds to the sample showing non metallic transport behavior.

The dependency of the electrical resistance on the external magnetic field for FeCo–TiO_2 composites with different MVF, measured at RT, is depicted in Fig. 7. The relative change in the resistance, called the magnetoresistance, is given by

$$\mathrm{MR} = \frac{[R(H) - R(_0)]}{R(_0)}$$

where $R(H)$ and $R(_0)$ are resistance measured in an applied magnetic field and zero magnetic field, respectively. All the films show a decrease in the resistance upon the application of an external magnetic field. A maximum change of 4% was measured for a composite with 48% MVF, within the range of applied field. The TMR was found to be present for amorphous as well as crystalline FeCo particles and higher for the later. As seen in Fig. 7, the TMR amplitude increases with increase in the MVF up to 48% and then decreases. The results for FeCo–TiO_2 reported here possess the same course of TMR as a function of FeCo volume fraction, as reported for aforementioned other granular films [9].

In the beginning, FeCo Particles are few and far apart, i.e., the thickness of oxide tunnel is larger than the spin diffusion length giving rise to smaller TMR amplitude. The TMR curves do not show hysteresis and are unsaturated. As the MVF advances, the metallic particles tend to grow in size, resulting in the decrease of inter-particle separation and we observed crystalline FeCo particles above 35% MVF. The still increasing TMR indicates that the grains are separate and an optimum configuration for spin dependent tunneling occurs at 48% MVF. In this context, it is difficult to determine in which proportion the change in inter-particle separation and the formation of crystalline particles contributes to the increase in TMR. Further increase in the MVF leads to coalescence between neighboring particles. Coalescences cause formation of clusters of particles with multidomain structure due to magnetic inter particle interaction which is reflected in butterfly-shaped TMR hysteresis (Fig. 8c, inset).

Inoue et al. [5] explained the change in electrical resistance for granular films by spin dependent tunneling of electrons between metal nanograins embedded in an insulating matrix. The magnetic moments of the granules in as-deposited composite films are randomly oriented at RT [22]. In the external magnetic field, the relative orientation of the magnetization between adjacent grains rotates into a parallel configuration causing increase in tunneling probability. For uniform size superparamagnetic particles with uncorrelated moments, the TMR ratio will be proportional to the square of the relative magnetization of the system, $\langle \cos\theta \rangle = m^2 (m = M/M_s)$ where M_s is the saturation magnetization [5]. Our experimental data for MVF 43 and 48% in Fig. 8 follow quite well the relation $\Delta R/R_0 \, \alpha \, -(M/M_s)^2$ implying spin dependent tunneling in FeCo–TiO_2 composite films. For fitting this relation with TMR curves, magnetization M at $H = 7.5$ KOe is taken as the saturation magnetization. The inset of Fig. 8a and b shows the quadratic behavior of magnetoresistance vs the global magnetization. However, as expected, the film with composition near to 53% MVF does not obey this quadratic law. At this

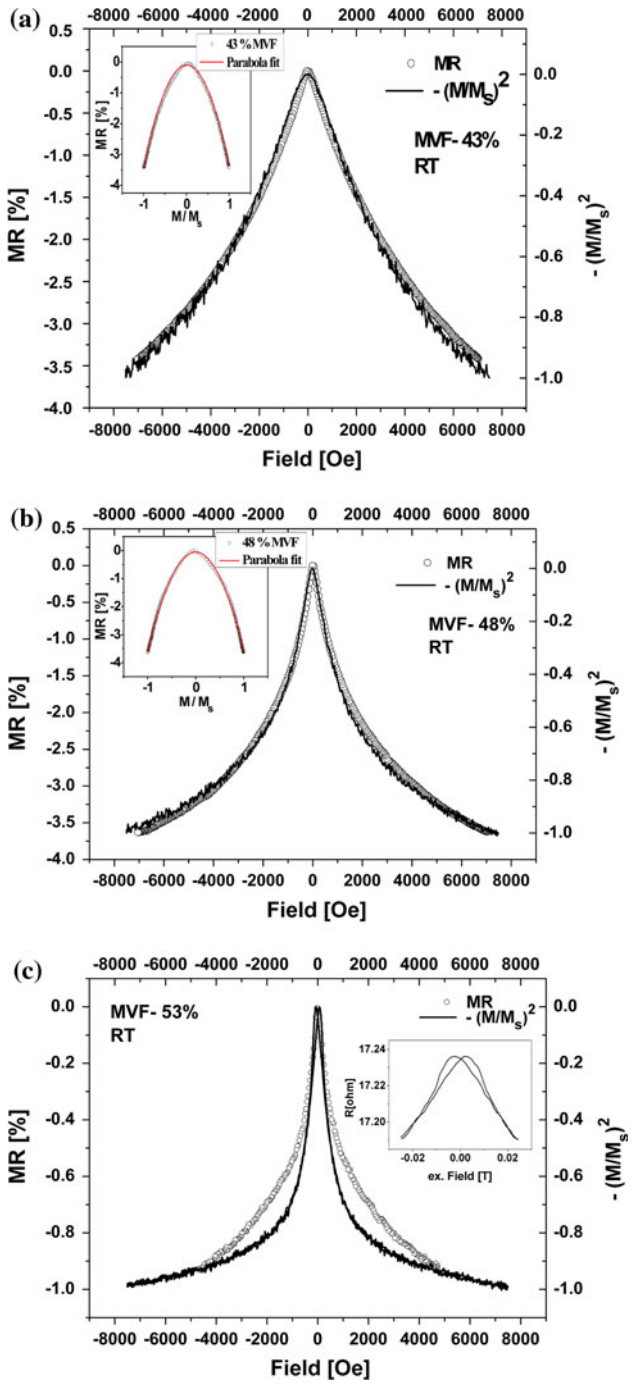

Fig. 8 TMR as a function of applied magnetic field and square of normalized magnetization, $(M/M_s)^2$ from VSM measurements at RT for **a** 43%, *inset* TMR versus magnetization, **b** 48%, *inset* TMR vs magnetization, and **c** 53% metal volume fractions. Figure 8c *inset*, appearance of hysteresis in TMR measurement in accordance with VSM measurement for 53% MVF

filling factor, the FeCo exhibits particle coalescence resulting in multi domain formation. The TMR amplitude rapidly drops and originates from the uncoupled small superparamagnetic particles still present, where as the magnetization is dominated by coalesced clusters.

Finally, we note that the TMR of granular structures is substantially lower than TMR values reported for the TMR devices fabricated by advanced lithography techniques involving epitaxial oxide layers [23, 24]. Nevertheless, due to simple fabrication process, the granular TMR approach is tempting for low-cost magnetic field sensors, where highest sensitivity is not required.

In conclusion, magnetic nanocomposites were prepared by sputtering of a FeCo alloy and TiO2. The microstructure of the nanocomposites was found to depend on the MVF. Films containing MVF up to 35% are marked by absence of any crystalline component whereas FeCo starts forming crystallites at MVF greater than 35%. Particle size distribution functions were obtained by fitting the experimental magnetization curves with Langevin function. Particle size and the volume fraction are closely related. The critical sizes where, the amorphous to crystalline and superparamagnetic to ferromagnetic transitions take place, are 1 nm and above 6 nm, respectively. TMR was observed in both the cases and a maximum of 4% for the 48% MVF film at room temperature.

Acknowledgements Financial support by the German Science Foundation (DFG) through the Collaborative Research Center (SFB) 677 "Function by Switching"—Project C7 is gratefully acknowledged. The authors thank Prof. Dr. Dr. h. c. Mult. A. Simon for enabling TEM experiments.

References

1. Gittleman J, Goldstein Y, Bozowski S (1972) Phys Rev B 5:3609
2. Helman JS, Abeles B (1976) Phys Rev Lett 37:1429
3. Fujimori H, Ohnuma S, Kobayashi S, Masumoto T (2006) J Magn Magn Mater 304:32
4. Ohnuma S, Ohnuma M, Fujimori H, Masumoto T (2007) J Magn Magn Mater 310:2503
5. Inoue J, Maekawa S (1996) Phys Rev B 53:R11927
6. Yakushiji K, Mitani K, Ernult F, Takanashi K, Fujimori H (2007) Phys Rep 451:1
7. Vovk A, Golub V, Malkinski L, Kravets A, Pogorily A, Shypil O (2004) J Magn Magn Mater 272
8. Wang C, Guo Z, Rong Y, Hsu TY (2004) Phys Stat Sol C 1(7):1736
9. Song HQ, Mei LM, Zhang YP, Yan SS, XL Ma, Wang Y, Zhang Z, Chen YL (2007) Phys B 388:130
10. Schürmann U, Hartung W, Takele H, Zaporojtchenko V, Faupel F (2005) Nanotechnology 16:1078
11. Takele H, Schuermann U, Greve H, Paretkar D, Zaporojtchenko V, Faupel F (2006) Eur Phys J Appl Phys 33:83
12. Bayliss P (1941) Trans Am Soc Met 29:415
13. Díaz-Ortiz A, Drautz R, Fähnle M, Dosch H, Sanchez JM (2006) Phys Rev B 73:224208
14. Owen EA, Madoc Jones D (1992) Proc Phys Soc B 67:456
15. Hattink B, García del Muro M, Konstantinović Z, Batlle X, Labarta A, Varela M (2006) Phys Rev B 73:045418
16. Honda S, Okada T, Nawate M, Tokumoto M (1997) Phys Rev B 56:22

17. O'Handley R (1999) Modern magnetic materials. Principles and applications. Wiley Interscience, New York
18. Xiao G, Chien C (1987) J Appl Phys 61:3308
19. Granquist C, Buhrman R (1976) J Appl Phys 47:2200
20. Gong W, Li H, Zhao Z, Chen J (1991) J Appl Phys 69(8):15
21. Leslie-Pelecky D, Rieke R (1996) Chem Mater 8:1773
22. Kwong H, Wong M, Wong Y, Wong K (2006) Appl Phy Lett 89:173109
23. Zhu J, Park C (2006) Mater Today 9:36
24. Parkin SSP, Kaiser C, Panchula A, Rice P, Hughes B, Samant M, Yang S-H (2004) Nat Mater 3:862